Experimental demonstration of the reverse flow catalytic membrane reactor concept for energy efficient syngas production. Part 2: Model development

J. Smit, G.J. Bekink, M. van Sint Annaland[*], J.A.M. Kuipers

Department of Science and Technology, University of Twente, P.O. Box 217, 7500 AE Enschede, The Netherlands

Abstract

A detailed reactor model has been developed to describe the experimental results that were obtained with the reverse flow catalytic membrane reactor (RFCMR) demonstration unit, presented in Part 1. The reactor model is based on a model that was used previously [Smit, J., van Sint 2005b. Annaland, M., Kuipers, J.A.M., 2005b. Feasibility study of a reverse flow catalytic membrane reactor with porous membranes for the production of syngas. Chemical Engineering Science 60(24), 6971–6982] to demonstrate the conceptual feasibility of the RFCMR concept at industrially relevant conditions. To accurately capture the radial heat losses and heat buffering effects in the RFCMR demonstration unit, the existing model has been extended with a detailed description of the two-dimensional heat transport in the insulation layer. By simulating a number of experimental cases discussed in Part 1, it is shown that the radial heat losses and therefore also the axial temperature profiles in the RFCMR demonstration unit can be very well described, without using any fitting parameters. Furthermore, it is shown that also the syngas composition can be predicted reasonably well by simply assuming local thermodynamic equilibrium. The very good agreement between the experimental results and the predictions of the reactor model clearly support the results of the conceptual feasibility study.
© 2006 Elsevier Ltd. All rights reserved.

Keywords: Chemical reactors; Membranes; Packed bed; Partial oxidation; Reactor modelling; Syngas

1. Introduction

The technical feasibility of the reverse flow catalytic membrane reactor (RFCMR) concept with porous membranes for energy efficient syngas production was investigated with a detailed experimental study in a demonstration unit in Part 1 of this contribution. In this second part, a reactor model is developed to describe the obtained experimental results. This model is based on the reactor model that was used previously to demonstrate the conceptual feasibility of the RFCMR concept at industrially relevant conditions (Smit et al., 2005b). The ultimate objective of the present study therefore is to validate

this reactor model with the experimental results obtained in the RFCMR demonstration unit and to show that the model used for the conceptual feasibility study can indeed describe an industrial scale reactor.

As was already discussed in Part 1 and also in a previous experimental study (Smit et al., 2005a), the axial temperature profiles in a lab-scale RFCMR demonstration unit are greatly affected by inevitable radial heat losses and heat buffering effects. Similar observations were made by van de Beld and Westerterp (1996) and Aubé and Sapoundjiev (2000) and these latter authors showed that the radial heat losses can be accurately captured by extending the reactor model with a two-dimensional description of the insulation layer. Therefore, a detailed description of the heat transport inside the insulation box will also be included in the reactor model used for the present study.

Firstly, the ability of the reactor model to describe the heat transport in the insulation box and the shell compartment will be validated with experimental results that were obtained in the

* Corresponding author. Tel.: +31 53 4894478; fax: +31 53 4892882.
E-mail address: M.VanSintAnnaland@tnw.utwente.nl (M. van Sint Annaland).

demonstration unit while operating it as a conventional reverse flow reactor (RFR) for the combustion of a small amount of CH_4 in air by removing the tube compartment, see Smit et al. (2005a). This approach has the advantage that additional complexity related to the modelling of the tube compartment of the RFCMR can be eliminated.

Subsequently, the reactor model will be further extended to include the description of the tube compartment of the RFCMR demonstration unit. With the reactor model a number of experimental cases studied in the RFCMR demonstration unit will be simulated. It will be shown that both the axial temperature profiles and the syngas compositions can be predicted very well without using any fitting parameters.

2. Reactor model: RFR

To describe the experimental results obtained by operating the RFCMR demonstration unit as a conventional RFR for the combustion of a small amount of CH_4 in air (Smit et al., 2005a), a detailed reactor model was developed. This model is based on the reactor model that was used for the conceptual feasibility study of the RFCMR concept with porous membranes at industrially relevant conditions (Smit et al., 2005b).

The axial temperature and concentration profiles in the O_2 and syngas compartments were modelled with a one-dimensional axial dispersion model. Radial temperature and concentration gradients inside the compartments were ignored to avoid excessive computational time. Radial temperature differences between the tube compartment, tube wall and shell compartment were accounted for via overall heat transfer coefficients. To describe the heat transfer processes in the tube and shell compartments of the reactor a homogeneous model (Vortmeyer, 1989) was adopted. The gas phase was assumed to be in pseudo-stationary-state because of the small gas phase residence time compared to the switching times, i.e., the accumulation terms in the species conservation equations were neglected and therefore also the switching losses.

To solve the system of strongly non-linear partial differential equations, an efficient numerical algorithm was used, which includes higher order discretisation schemes for the accumulation and convection terms and automatic time step and local grid adaptation, see Smit et al. (2005c) for details.

Because of the relatively large specific external surface area and the accompanying large radial heat losses of the RFCMR demonstration unit and also because of the heat buffering effect of the insulation box, it was found that it is essential to incorporate a description of the radial heat losses into the model. Therefore, the reactor model was extended with a detailed description of the heat transport inside the insulation box, following Aubé and Sapoundjiev (2000). It was assumed that the insulation box can be represented by a cylinder with a diameter equal to the height of the box. This approximation can be justified, since the main resistance for the heat transport and hence the largest temperature gradients are located close to the shell wall, whereas the temperature gradients at the surface of the insulation box are very flat. The insulation layer can thus be described by a two-dimensional model (cylindrical coordinates), which was solved explicitly in the radial direction and implicitly in the axial direction to allow for local grid adaptation in the axial direction.

The mass and energy conservation equations of the RFR model are given in Table 1. For the boundary conditions the usual Danckwerts-type approach was used. In Table 2, the correlations that were used to compute the heat and mass transfer coefficients are given. The thermal conductivity of the quiescent packed bed was calculated according to Zehner and Schlünder (1970) and the wall-to-bed heat transfer coefficient following Dixon and Creswell (1979), but the lengthy equations are omitted here (see also Smit, 2006, for details). The axial pressure drops over the tube and shell compartments were calculated with the differential form of the Ergun-equation (Ergun, 1952),

$$-\frac{\partial p}{\partial z} = 150\left(\frac{\eta_g v_g}{d_p^2}\right)\frac{(1-\varepsilon_g)^2}{\varepsilon_g^3} + 1.75\left(\frac{\rho v_g^2}{d_p}\right)\frac{1-\varepsilon_g}{\varepsilon_g^3}. \quad (13)$$

The heat transfer coefficient from the outer surface of the insulation box to the air was approximated via a Nusselt correlation for laminar natural convection near a hot vertical plate (Bird et al., 2002),

$$\alpha^{i--\text{air}} = 0.515\frac{\lambda_{g,\text{air}}}{h^i}(Ra^{i-\text{air}})^{1/4}, \quad (14)$$

where the Rayleigh number is given by

$$Ra^{i-\text{air}} = gPr\left(h^i\right)^3\frac{T^i - T^{\text{air}}}{T^{\text{air}}}\left(\frac{\rho_{g,\text{air}}}{\eta_{g,\text{air}}}\right)^2. \quad (15)$$

The heat transfer coefficient from the outer ends of the shell (i.e., outside the insulation box, see Part 1, Fig. 6) to the air was approximated via the Rayleigh number for laminar natural convection around a hot horizontally placed cylinder (Bird et al., 2002),

$$\alpha^{sw-\text{air}} = 0.398\frac{\lambda_{g,\text{air}}}{2R_o^s}(Ra^{sw-\text{air}})^{1/4}, \quad (16)$$

where

$$Ra^{sw-\text{air}} = gPr(2R_o^s)^3\frac{T^{sw} - T^{\text{air}}}{T^{\text{air}}}\left(\frac{\rho_{g,\text{air}}}{\eta_{g,\text{air}}}\right)^2. \quad (17)$$

Although the actual heat transfer from the bottom and top of the insulation box to the air is different than from a vertical plate, approximating the total heat transfer from the insulation box to the air by considering the box as a cylinder with a single heat transfer coefficient is sufficiently accurate for our purposes. This is because the main heat transfer resistance in the insulation box is situated near the shell surface in the centre of the box rather than at the outer surface of the box, as was discussed earlier.

To describe the combustion of a small amount of CH_4 in air over a Pt/Al_2O_3 combustion catalyst, the kinetic rate expression determined by van Sint Annaland (2000) was used

$$R^s = \rho_{\text{cat}}^s k^s \exp\left(-\frac{E_a^s}{R_g T^s}\right)c_{O_2,g}^s c_{CH_4,g}^s. \quad (18)$$

Table 1
Conservations equations of the reactor model of the RFCMR demonstration unit operated as RFR

Mass conservation equations

$$\frac{\partial(\rho_g^s v_g^s)}{\partial z} = 0 \tag{1}$$

$$\rho_g^s v_g^s \frac{\partial w_{\mathrm{CH4},g}^s}{\partial z} = \frac{\partial}{\partial z}\left(\rho_g^s D_{\mathrm{ax}}^s \frac{\partial w_{\mathrm{CH4},g}^s}{\partial z}\right) + r_{\mathrm{CH4},g}^s \tag{2}$$

Energy conservation equations
Shell

$$(\varepsilon_g^s \rho_g^s C_{p,g}^s + \rho_{\mathrm{bulk}}^s C_{p,s}^s)\frac{\partial T^s}{\partial t} = -\rho_g^s v_g^s C_{p,g}^s \frac{\partial T^s}{\partial z} + \frac{\partial}{\partial z}\left(\lambda_{\mathrm{eff}}^s \frac{\partial T^s}{\partial z}\right) - \sum_j \frac{r_{j,g}^s}{M_j} H_{j,g}^s + \frac{2\pi}{R_i^s}\alpha^{s--sw}(T^{sw} - T^s) \tag{3}$$

Shell wall, inside the insulation box

$$\rho_s^{sw} C_{p,s}^{sw} \frac{\partial T^{sw}}{\partial t} = \frac{\partial}{\partial z}\left(\lambda_s^{sw}\frac{\partial T^{sw}}{\partial z}\right) + \frac{2R_i^s \alpha^{s--sw}}{(R_o^s)^2 - (R_i^s)^2}(T^s - T^{sw}) + \frac{2R_o^s \alpha^{sw--i}}{(R_o^s)^2 - (R_i^s)^2}(T_{z,r=R_o^i}^i - T^{sw}) \tag{4}$$

Shell wall, outside the insulation box

$$\rho_s^{sw} C_{p,s}^{sw} \frac{\partial T^{sw}}{\partial t} = \frac{\partial}{\partial z}\left(\lambda_s^{sw}\frac{\partial T^{sw}}{\partial z}\right) + \frac{2R_i^s \alpha^{s--sw}}{(R_o^s)^2 - (R_i^s)^2}(T^s - T^{sw}) + \frac{2R_o^s \alpha^{sw--\mathrm{air}}}{(R_o^s)^2 - (R_i^s)^2}(T^{\mathrm{air}} - T^{sw}) \tag{5}$$

Insulation layer

$$\rho_s^i C_{p,s}^i \frac{\partial T^i}{\partial t} = \frac{\partial}{\partial z}\left(\lambda_s^i \frac{\partial T^i}{\partial z}\right) + \frac{1}{r}\frac{\partial}{\partial r}\left(r\lambda_s^i \frac{\partial T^i}{\partial r}\right) \tag{6}$$

Boundary conditions, insulation layer

$$\lambda_s^i \frac{\partial T^i}{\partial r}\bigg|_{z,r=R_o^s} = \alpha^{sw--i}(T^{sw} - T^i)|_{z,r=R_o^s}, \quad \lambda_s^i \frac{\partial T^i}{\partial r}\bigg|_{z,r=R_o^i} = \alpha^{i--\mathrm{air}}(T^{\mathrm{air}} - T^i)|_{z,r=R_o^i} \tag{7}$$

$$\lambda_s^i \frac{\partial T^i}{\partial z}\bigg|_{z=Z_0^i,r} = \alpha^{i--\mathrm{air}}(T^{\mathrm{air}} - T^i)|_{z=Z_0^i,r}, \quad \lambda_s^i \frac{\partial T^i}{\partial z}\bigg|_{z=Z_L^i,r} = \alpha^{i--\mathrm{air}}(T^{\mathrm{air}} - T^i)|_{z=Z_L^i,r} \tag{8}$$

Table 2
Heat and mass transfer coefficients

Gas-to-particle heat transfer coefficient (Gunn, 1978)

$$Nu = (7 - 10\varepsilon_g + 5\varepsilon_g^2)(1 + 0.7Re^{0.2}Pr^{1/3}) + (1.33 - 2.4\varepsilon_g + 1.2\varepsilon_g^2)Re^{0.7}Pr^{1/3} \tag{9}$$

Axial heat dispersion (Gunn and Misbah, 1993)

$$\lambda_{\mathrm{eff}} = \lambda_{\mathrm{bed}} + \frac{Re\,Pr\,\lambda_g}{Pe_{\mathrm{ax}}} + \frac{Re^2 Pr^2 \lambda_g}{6(1-\varepsilon_g)Nu}, \quad Pe_{\mathrm{ax}} = \frac{2p}{1-p}, \quad p = 0.17 + 0.33\exp\left(\frac{-24}{Re}\right) \tag{10}$$

Gas-to-particle mass transfer coefficient (Thoenes and Kramers, 1958)

$$k_g = \frac{0.81}{\varepsilon_g}v_g Re^{-0.5}Sc^{-2/3} \tag{11}$$

Axial mass dispersion coefficient (Edwards and Richardson, 1968)

$$\frac{D_{\mathrm{ax}}}{v_g d_p} = \frac{0.73}{Re\,Sc} + \frac{0.5}{1 + 9.7\varepsilon_g Re\,Sc} \tag{12}$$

Table 3
Physical properties of vermiculite and stainless steel

	Vermiculite[a]	Stainless steel[b]
$C_{p,s}$ (J/kg/K)	960	$-1.73 \times 10^{-4} T^2 + 0.406T + 365$
$d_{p,s}$ (m)	3.5×10^{-3}	
e_s	0.65	0.65
λ_s (J/m/K/s)	$1.40 \times 10^{-4} T - 1.12 \times 10^{-2} + 2.27 \times 10^{-7} \dfrac{e_s^i}{2 - e_s^i} T^3 d_s^i$	$1.53 \times 10^{-2} T + 9.02$
ρ_s (kg/m^3)	182	7750

[a]Data from manufacturer (T in K).
[b]Karditsas and Baptiste (2005) (T in K).

Because only a small amount of CH_4 is combusted, the reaction rate $r_{CH_4,g}^s$ in Eq. (2) can be considered to be pseudo-first order with respect to CH_4, so that the effective reaction rate including internal and external mass transfer can be calculated analytically (Westerterp et al., 1984):

$$r_{CH_4,g}^s = \frac{-M_{CH_4}}{\dfrac{d_{p,\text{cat}}^s}{6c_{CH_4,g}^s k_g (1 - \varepsilon_g)} + \dfrac{1}{R^s \eta}}. \tag{19}$$

The effectiveness factor η is calculated with

$$\eta = \frac{3\varphi - \tanh(3\varphi)}{3\varphi^2 \tanh(3\varphi)}. \tag{20}$$

The Thiele modulus φ is given by

$$\varphi = \frac{d_{p,\text{cat}}^s}{6} \sqrt{\frac{k_\eta}{D_{\text{eff}}}}, \tag{21}$$

where

$$k_\eta = \rho_{\text{cat}}^s k^s \exp\left(-\frac{E_a^s}{R_g T^s}\right) c_{O_2,s}^s. \tag{22}$$

The effective diffusivity D_{eff} in Eq. (21) is calculated via Blanc's law (Reid et al., 1987) and the Knudsen diffusivity:

$$\frac{\varepsilon_s}{\tau D_{\text{eff}}} = \frac{1}{D_j} + \frac{1}{D_{KN}} = \frac{1}{\dfrac{1}{\sum_i \dfrac{x_i}{D_{i,j}}}} + \frac{1}{\dfrac{2}{3} r_p \sqrt{\dfrac{8 R_g T}{\pi \langle M \rangle}}}. \tag{23}$$

For fresh catalyst particles the kinetic data obtained by van Sint Annaland (2000) could accurately describe the experimental results. However, because of the relatively high temperatures in the demonstration unit, it was found that the activity of the catalyst quickly decreased because of sintering and loss of Pt due to vapourisation until a relatively constant activity was observed. For the aged catalyst the Pt loading was found to be 0.4% and the specific surface area had decreased to 44 m^2/g (see Part 1 for the fresh catalyst properties). Therefore, the lumped kinetics of the combustion reaction were measured for the aged catalyst. The activation energy and pre-exponential factor were determined as 168 kJ/mol and 1.071×10^7 m^6/kg/s/mol, respectively. The experimental results and a detailed description of the experimental set-up and procedures can be found in Appendix A.

Table 4
Physical properties catalyst

E_a^s (kJ/mol)	168
k^s (m^6/kg/s/mol)	1.071×10^7
r_p (m)	9.1×10^{-9}
$d_{p,\text{cat}}^s$ (m)	0.003
ε_g	0.4
ε_s	0.6
ρ_{cat}^s (kg/m^3)	677
τ	2

The physical properties of the insulation material and stainless steel have been summarised in Table 3. In the calculation of the thermal conductivity of the vermiculite, the heat transport due to radiation was super-imposed. The physical properties of the catalyst are summarised in Table 4. Other physical properties were calculated according to Reid et al. (1987), using the pure component data tabulated by Daubert and Danner (1985).

3. Model validation: RFR

With the reactor model, simulations were carried out for three cases in which the RFCMR demonstration unit was operated as RFR for the combustion of a small amount of CH_4 in air, as reported by Smit et al. (2005a). The related operating conditions are listed in Table 5. The measured axial temperature profile at the beginning of the experiment (after heating up) was taken as initial condition for the temperature profile in the shell to speed up the computations. Furthermore, the insulation layer in the reactor model was allowed to heat up for 7200 s before applying the gas flows, in order to establish a temperature profile in the insulation layer very similar to the actual temperature profile

Table 5
Operating conditions used in the RFCMR demonstration unit operated as RFR for CH_4 combustion in air for different cases

	A	B	E
L_{Pt/Al_2O_3} (m)	0.3	0.3	0.3
t_{switch} (s)	120	240	120
T_{feed} (K)	298	298	298
$\phi_{v,\text{total,in}}^s$ (l/min, STP)	30	30	20
$x_{CH_4,\text{in}}^s$	0.018	0.018	0.018

in the insulation box. It was confirmed with other calculations that the same cyclic steady state was obtained when assuming a uniform temperature profile above the ignition temperature as initial temperature profile. It was found that the measured axial temperature profiles in the RFCMR demonstration unit operated as RFR could be very well described by the reactor model. This is illustrated for case B in Fig. 1, where the measured and simulated axial temperature profiles are given at several moments in time. At each moment the height of the temperature plateau, the steepness of the temperature fronts as well as the front velocity agree very well, even after almost 3 h of operation.
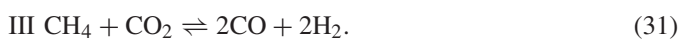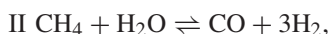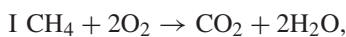
In Fig. 2 the measured and predicted axial temperature profiles after 9600 s are given for cases A and E. Also for case A the model corresponds very well with the measured temperature profiles, but for case E the agreement is somewhat less and the heat losses appear to be underestimated, although the temperature plateaus and front velocities are still very similar.

The discrepancy for case E may have been caused by the lower flow rate used in case E, so that radial heat losses and an accurate description of these heat losses become more important. Another reason could be the presence of radial concentration and temperature gradients (not taken into account in the reactor model), because of which the ignition of the CH_4 combustion is postponed. To improve the accuracy a complete two-dimensional model should be used to also describe the radial temperature and concentration profiles inside the tube and shell compartments (Aubé and Sapoundjiev, 2000), but such a model is much more CPU demanding, especially for the RFCMR because of the large number of equations that have to be solved simultaneously. Nevertheless, in view of the uncertainties in the physical properties, constitutive relations and reaction kinetics, the reactor model is able to describe the experiments very well, without using any fitting parameters.

4. Reactor model: RFCMR

To describe the experimental results of the RFCMR demonstration unit, the reactor model of the RFR was extended with a detailed description of the phenomena prevailing in the tube compartment. The mass and energy conservation equations describing the shell and tube compartments and the tube wall are given in Table 6.

For the partial oxidation reactions local, instantaneous equilibrium was assumed inside the filter, but solid carbon (i.e., coke formation) was not taken into account. In this case the local equilibrium syngas composition can be described by three independent reactions, full combustion of CH_4, steam reforming of CH_4 and CO_2 reforming of CH_4:

$$\text{I} \quad CH_4 + 2O_2 \rightarrow CO_2 + 2H_2O,$$

$$\text{II} \quad CH_4 + H_2O \rightleftharpoons CO + 3H_2,$$

$$\text{III} \quad CH_4 + CO_2 \rightleftharpoons 2CO + 2H_2. \tag{31}$$

In the reactor model the local equilibrium compositions were calculated by using equilibrium kinetics for reactions I–III

$$R_{\text{I}}^t = k_{\text{I},\infty}^t p_{O_2}^t p_{CH_4}^t, \tag{32}$$

$$R_{\text{II}}^t = k_{\text{II},\infty}^t \left(p_{CH_4}^t p_{H_2O}^t - \frac{(p_{H_2}^t)^3 p_{CO}^t}{(p_g^\ominus)^2 K_{\text{eq,II}}} \right), \tag{33}$$

$$R_{\text{III}}^t = k_{\text{III},\infty}^t \left(p_{CH_4}^t p_{CO_2}^t - \frac{(p_{H_2}^t)^2 (p_{CO}^t)^2}{(p_g^\ominus)^2 K_{\text{eq,III}}} \right). \tag{34}$$

For the k_∞ a very high value was used so that eventually the terms between brackets in Eqs. (33)–(34) approach zero and local equilibrium is attained. The different r_j in Table 6, Eq. (27) can be directly calculated from Eqs. (32)–(34):

$$r_{CH_4,g}^t = M_{CH_4}(-R_{\text{I}}^t - R_{\text{II}}^t - R_{\text{III}}^t),$$
$$r_{CO,g}^t = M_{CO}(R_{\text{II}}^t + 2R_{\text{III}}^t),$$
$$r_{CO_2,g}^t = M_{CO_2}(R_{\text{I}}^t - R_{\text{III}}^t),$$
$$r_{H_2,g}^t = M_{H_2}(3R_{\text{II}}^t + 2R_{\text{III}}^t),$$
$$r_{H_2O,g}^t = M_{H_2O}(2R_{\text{I}}^t - R_{\text{II}}^t),$$
$$r_{O_2,g}^t = M_{O_2}(-2R_{\text{I}}^t). \tag{35}$$

The total permeation rate through the holes of the filter could ideally be approximated with the well-known Hagen–Poiseuille equation (Bird et al., 2002) by considering a single hole as a perfect cylindrical tube

$$J = \frac{p^t + p^s}{2R_g T^{tw}} \frac{n_h R_h^4 (p^s - p^t)}{16 R_i^t L_{\text{filter}} \eta_g^s L_h}. \tag{36}$$

However, the permeation rate through the filter was greatly over-predicted by this equation. This is probably caused by the roughness of the steel surface and also by additional friction at the in- and outlet of the holes. To account for the additional friction and to calculate pressure differences with the reactor model, which correspond with the measured pressure differences, the friction factor was increased by a factor of 16.

During the simulation study, it was found that the axial pressure drop in the tube compartment calculated with the reactor model was considerably larger than observed during the experiments, very likely because of the very low tube diameter to particle diameter ratio (about 2) in the RFCMR demonstration unit. In the RFCMR reactor model the axial pressure drop was computed with the Ergun Equation (13), which is not very accurate for these low ratios. To account for the low tube diameter to particle diameter ratio and to calculate axial pressured drops with the reactor model, which are similar to those measured in the RFCMR demonstration unit, the friction factors were reduced, which corresponded to doubling the particle diameter.

5. Model validation: RFCMR

With the reactor model of the RFCMR demonstration unit, simulations were carried out using the operating conditions of
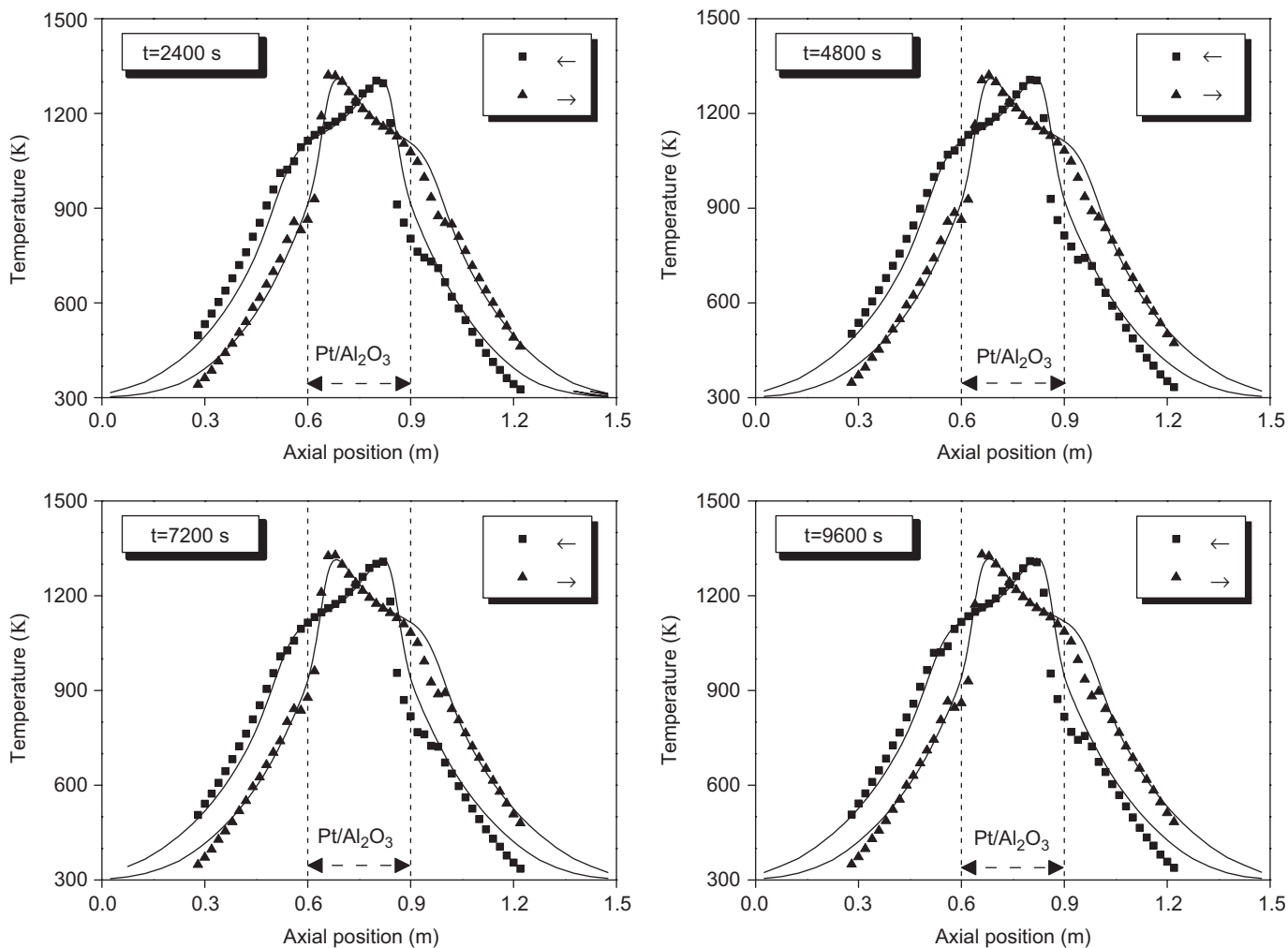
Fig. 1. Measured (markers) and predicted (solid lines) axial temperature profiles in the RFCMR demonstration unit operated as RFR after a forward ($\rightarrow$) and backward ($\leftarrow$) semi-cycle at several moments in time (case B).
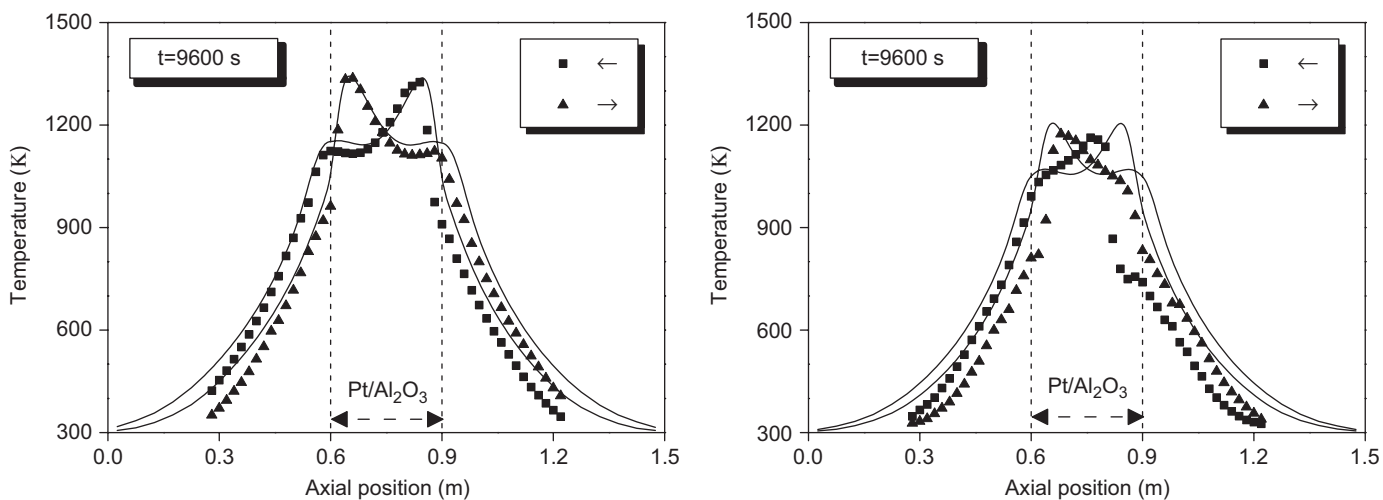

Fig. 2. Measured (markers) and predicted (solid lines) axial temperature profiles in the RFCMR demonstration unit operated as RFR after a forward ($\rightarrow$) and backward ($\leftarrow$) semi-cycle after 9600 s for cases A (left) and E (right).

Table 6
Conservation equations for the tube and shell compartments and the tube wall in the reactor model of the RFCMR demonstration unit

Mass conservation equations

$$\frac{\partial(\rho_g^s v_g^s)}{\partial z} = -\langle M^s \rangle \frac{2R_i^t}{(R_i^s)^2 - (R_o^t)^2} J \tag{24}$$

$$\frac{\partial(\rho_g^t v_g^t)}{\partial z} = \langle M^s \rangle \frac{2}{R_i^t} J \tag{25}$$

$$\rho_g^s v_g^s \frac{\partial w_{j,g}^s}{\partial z} = \frac{\partial}{\partial z}\left(\rho_g^s D_{ax}^s \frac{\partial w_{j,g}^s}{\partial z}\right) + r_{j,g}^s \tag{26}$$

$$\rho_g^t v_g^t \frac{\partial w_{j,g}^t}{\partial z} = \frac{\partial}{\partial z}\left(\rho_g^t D_{ax}^t \frac{\partial w_{j,g}^t}{\partial z}\right) + r_{j,g}^t + (1 - w_{j,g}^s)\langle M^s \rangle \frac{2}{R_i^t} J \tag{27}$$

Energy conservation equations

$$(\varepsilon_g^s \rho_g^s C_{p,g}^s + \rho_{bulk}^s C_{p,s}^s)\frac{\partial T^s}{\partial t} = -\rho_g^s v_g^s C_{p,g}^s \frac{\partial T^s}{\partial z} + \frac{\partial}{\partial z}\left(\lambda_{eff}^s \frac{\partial T^s}{\partial z}\right) - \sum_j \frac{r_{j,g}^s}{M_j} H_{j,g}^s + \frac{2R_o^t \alpha^{s-tw}}{(R_i^s)^2 - (R_o^t)^2}(T^{tw} - T^s) + \frac{2R_i^s \alpha^{s-sw}}{(R_i^s)^2 - (R_o^t)^2}(T^{sw} - T^s) \tag{28}$$

$$(\varepsilon_g^t \rho_g^t C_{p,g}^t + \rho_{bulk}^t C_{p,s}^t)\frac{\partial T^t}{\partial t} = -\rho_g^t v_g^t C_{p,g}^t \frac{\partial T^t}{\partial z} + \frac{\partial}{\partial z}\left(\lambda_{eff}^t \frac{\partial T^t}{\partial z}\right) - \sum_j \frac{r_{j,s}^t}{M_j} H_{j,g}^t + \frac{2\alpha^{t-tw}}{R_i^t}(T^{tw} - T^t) \tag{29}$$

$$\rho_s^{tw} C_{p,s}^{tw} \frac{\partial T^{tw}}{\partial t} = \frac{\partial}{\partial z}\left(\lambda^{tw} \frac{\partial T^{tw}}{\partial z}\right) + \frac{2R_o^t \alpha^{s-tw}}{(R_o^t)^2 - (R_i^t)^2}(T^s - T^{tw}) + \frac{2R_i^t \alpha^{t-tw}}{(R_o^t)^2 - (R_i^t)^2}(T^t - T^{tw}) \tag{30}$$

cases F, H and K listed in Table 1 in Part 1 of this contribution. Again the axial temperature profile measured at the beginning of the experiment was taken as initial condition for the simulation and before applying the gas flows, the insulation layer was allowed to heat up for 7200 s. In this section firstly the axial temperature profiles will be discussed and subsequently the syngas compositions.

5.1. Axial temperature profiles

In Fig. 3 the measured axial temperature profiles in the RFCMR demonstration unit and the simulated axial temperature profiles in the shell and tube compartments are given at the end of a forward and backward semi-cycle in the cyclic steady state (after 7200 s) for cases F, H and K. Because the temperatures were measured just outside the tube wall in the demonstration unit, the measured values should lie between the simulated values of the shell and tube compartments, but closer to those of the shell compartment. As shown in Fig. 3, the simulated temperature profiles correspond very well with the measured temperature profiles, especially the temperature fronts, the front velocities and the plateau temperatures, and indeed the measured values are closer to those computed for the shell compartment than to those computed for the tube compartment.

For case F pronounced temperature peaks due to CH_4 combustion in the shell compartment were observed in the measured axial temperature profiles at the end of each semi-cycle,

but according to Fig. 3 these peaks are not predicted by the reactor model. However, just after the beginning of a semi-cycle temperature peaks actually were predicted, which followed the measured peaks quite closely. About half-way the semi-cycle the computed temperature peaks started to decrease in time and at the end of the semi-cycle the peaks had completely disappeared. In the experiments it was observed that the temperature peaks maintained more or less the same height during the entire semi-cycle and traversed into the combustion catalyst bed.

The disagreement between the reactor model predictions and experimental results is probably caused by the presence of radial concentration and temperature gradients in the shell compartment, which are not taken into account in the reactor model. In the simulation the temperature at the beginning of the combustion catalyst bed apparently becomes too low in the second half of the semi-cycle to maintain a temperature peak at the beginning of the combustion catalyst bed, because locally not enough heat is produced anymore to counterbalance the heat convection. Nonetheless, still some CH_4 is converted at the beginning of the catalyst bed so that further on in the catalyst bed not enough CH_4 can be converted locally to form a temperature peak there instead.

In the experiments the temperature close to the shell wall at the beginning of the combustion catalyst bed might have become below the ignition temperature due to radial heat losses that no CH_4 is converted anymore in this part of the shell compartment. Instead, the ignition of the CH_4 combustion is
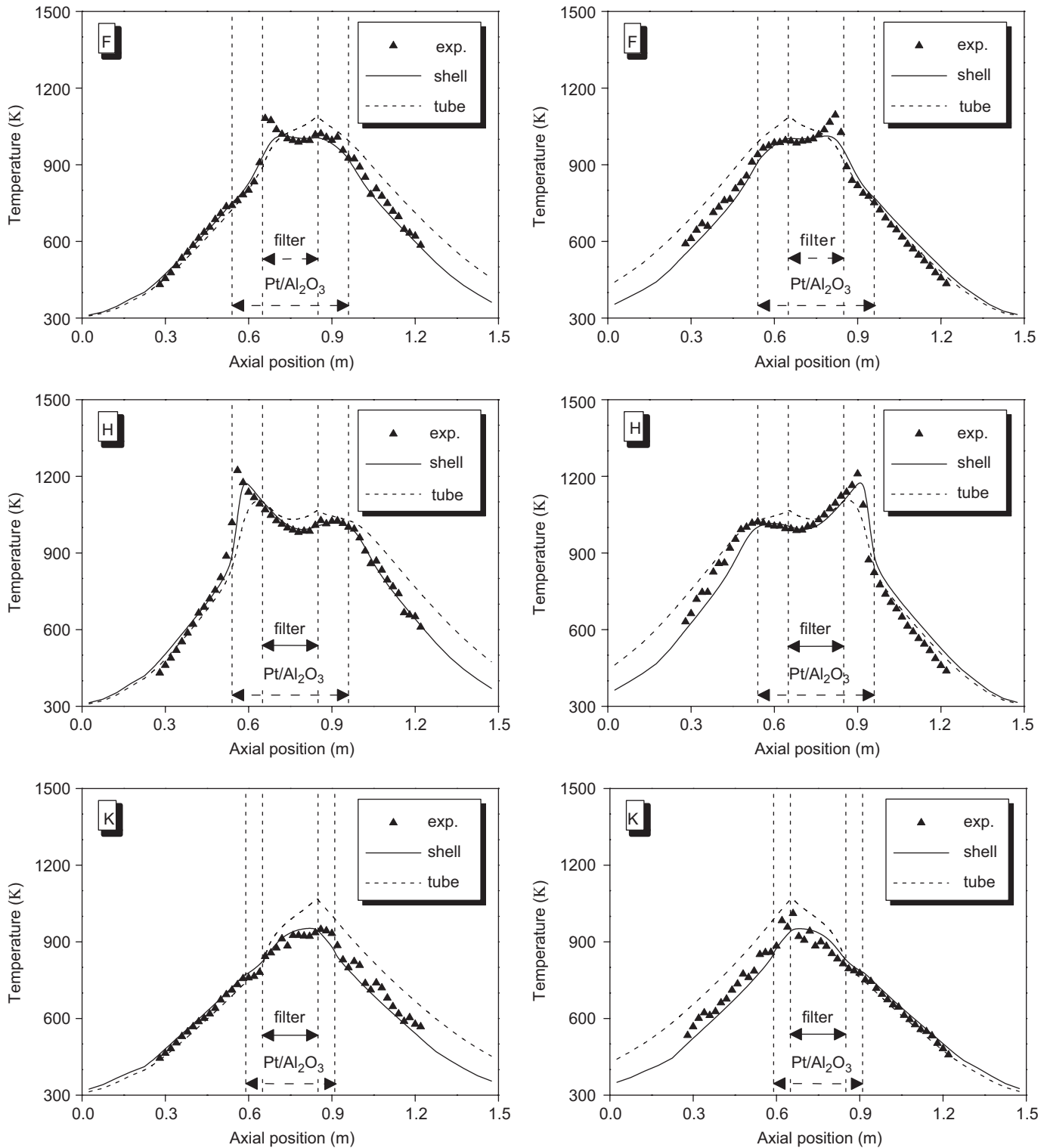
Fig. 3. Measured (markers) and simulated (lines) axial temperature profiles in the RFCMR demonstration unit at the end of forward (left) and backward (right) semi-cycle after 7200 s for cases F, H and K.

postponed so that still a temperature peak can be formed further on in the catalyst bed.

To verify this explanation, simulations with a full two-dimensional description of the tube and shell compartments

would be required, but this type of simulation is very CPU demanding, especially for the RFCMR because of the large number of equations to be solved for many time steps as discussed earlier, and hence such simulations were not

Table 7
Measured and simulated dry, normalised syngas compositions in the RFCMR demonstration unit and related quantities for cases F, H and K

	F		H		K	
	Exp.	Model	Exp.	Model	Exp.	Model
$x^t_{CH_4,out}$	0.049	0.035	0.058	0.046	0.042	0.041
$x^t_{CO,out}$	0.308	0.317	0.293	0.312	0.315	0.313
$x^t_{CO_2,out}$	0.021	0.012	0.029	0.015	0.018	0.015
$x^t_{H_2,out}$	0.614	0.636	0.619	0.627	0.625	0.630
$S^t_{CO,out}(\%)$	93.6	96.4	91.1	95.5	94.6	95.5
$S^t_{H_2,out}(\%)^a$	94.3	96.5	96.4	95.9	93.7	95.8
$R^t_{O_2/CH_4,out}{}^a$	0.513	0.499	0.492	0.494	0.524	0.502
$R^t_{H_2/CO,out}$	2.02	2.00	2.12	2.01	1.98	2.01
$\zeta^t_{CH_4,out}(\%)$	87.1	90.3	84.6	87.7	88.7	88.9

[a]Calculated from the overall mass balance.

included in this work. For case H and also for the cases studied with the conventional RFR the agreement between the simulated and measured axial temperature profile is much better. Apparently for these cases an accurate description of the radial concentration and temperature gradients is of less importance.

5.2. Syngas composition

In Table 7 the measured and simulated syngas compositions at the tube outlet of the demonstration unit are compared. The CH_4, CO, CO_2 and H_2 mole fractions were again normalised by excluding N_2 and time-averaged over multiple semi-cycles, excluding the first 40 s of every semi-cycle, see Part 1. Furthermore, also the CO and H_2 selectivities, the O_2/CH_4 and H_2/CO ratios and the CH_4 conversions have been included in Table 7.

The simulation results agree reasonably well with the experimental data indicating that the temperature profile in the filter is well described and that there are no significant kinetic and mass transfer limitations, which justifies the assumption of local thermodynamic equilibrium. However for cases F and H the measured CO selectivity is 3–5% lower than the simulated value. This is most likely because of the relatively slow CO_2 reforming of CH_4 while having assumed local thermodynamic equilibrium in the simulations and accordingly also the CH_4 conversions are slightly lower.

For an industrial-scale reactor with the amount of CH_4 that has to be added to the air feed to create the desired trapezoidal temperature profile is much smaller than for the lab-scale reactor used in this study and therefore the CO selectivity will be higher, since much less CO_2 from the air compartment has to be converted via slow dry reforming. This is confirmed by case K, in which no CH_4 is added to the air feed and where the difference between the measured and calculated CO selectivity is only about 1%. The differences between the mea-

sured and calculated H_2 selectivities are only about 2% and for case H the measured value is in fact higher than the calculated value.

In view of the strong temperature dependency of the equilibrium compositions at the temperatures studied and the steep radial temperature gradients, it is questionable if a more detailed description of the mass transfer and more detailed reaction kinetics would give a better agreement between the experimental and simulated results. Because of the extremely high partial oxidation reaction rates on Rh-based catalysts, it is very difficult to determine detailed reaction kinetics experimentally and up till now very few, if any, reaction kinetics of partial oxidation reactions on Rh-based catalysts have been reported in the literature. On the other hand, due to the fact that Rhodium is very expensive, for industrial applications probably a lower metal loading will be used and then kinetic and mass transfer limitations (and a detailed description thereof in a reactor model) could be much more important.

6. Conclusions

In order to describe the experimental results obtained in the RFCMR demonstration unit discussed in Part 1 of this contribution, a detailed reactor model was developed. For this purpose, the reactor model used in a previous study on the conceptual feasibility of the RFCMR concept for industrially relevant conditions (Smit et al., 2005a) was extended with a detailed description of the insulation box surrounding the reactor to accurately capture the inevitable radial heat losses and heat buffering effects. Furthermore, the reaction kinetics of CH_4 combustion in air were experimentally determined.

The reactor model was firstly compared with experimental results where the RFCMR demonstration unit was operated as a conventional RFR (Smit et al., 2005a) for CH_4 combustion in air to determine the ability of the model to capture the radial heat losses. It was found that the measured axial temperature profiles (and hence the radial heat losses) could be predicted very well provided that the flow rates are sufficiently large.

Subsequently, the reactor model was used to simulate a number of experimental cases studied in the RFCMR demonstration unit (Part 1). Again it was found that the measured axial temperature profiles in the demonstration unit could be predicted very well. Also the syngas compositions could be predicted reasonably well by simply assuming local thermodynamic equilibrium, although the CO and H_2 selectivity and the CH_4 conversion were generally slightly over-predicted.

Based on the very good agreement between the experimental results and the predictions of the reactor model, it can be concluded that the reactor model, which was used to demonstrate the conceptual feasibility of the RFCMR concept for industrially relevant conditions, gives a very realistic representation of an industrial scale reactor and that with high confidence the very high syngas selectivities that were calculated can indeed be achieved in practice.

Notation

A	pre-exponential factor, $m^6/kg/s/mol$
c_j	concentration of species j, mol/m^3
C_p	heat capacity, $J/kg/K$
d_p	particle diameter, m
D	diffusivity, m^2/s
D_{ax}	axial dispersion coefficient, m^2/s
D_{eff}	effective diffusivity, m^2/s
$D_{i,j}$	binary diffusion coefficient, m^2/s
$\overline{D}_j$	diffusivity of species j in a mixture, m^2/s
D_{KN}	Knudsen diffusivity, m^2/s
e	emissivity
E_a	activation energy, J/mol
g	acceleration by gravity, m/s^2
h^i	height insulation box, m
H_j	enthalpy of species j, J/mol
J	permeation rate, $mol/m^2/s$
k	reaction rate constant, $m^6/kg/s/mol$
k_∞	equilibrium reaction rate constant, $1/s$
k_η	linearised reaction rate constant, $1/s$
K_{eq}	equilibrium constant
L	length, m
L_{filter}	length of the filter, m
L_{Pt/Al_2O_3}	length combustion catalyst section, m
m	mass, kg
M	molar weight, kg/mol
n_h	number of holes
Nu	dimensionless Nusselt number, $\alpha_{g-s}d_p/\lambda_g$
p	parameter in axial heat dispersion coefficient of Gunn and Misbah (1993)
p	pressure, Pa
Pe_{ax}	dimensionless Péclet number for axial heat dispersion, $\rho_g v_g d_p C_{p,g}/\lambda_{ax}$
Pr	dimensionless Prandtl number, $C_{p,g}\eta_g/\lambda_g$
r	radial coordinate, m
r_j	reaction rate of species j, $kg/m^3/s$
r_p	pore radius, m
R	reaction rate, $mol/m^3/s$
R	radius, m
R_g	gas constant, $8.314\,J/mol/K$
$R_{j,k}$	molar ratio of species j to k
Ra	dimensionless Rayleigh number
Re	dimensionless Reynolds number, $\rho_g v_g d_p/\eta_g$
S	selectivity
Sc	dimensionless Schmidt number, $\eta_g/\rho_g/D$
t_{switch}	switching time, s
T	temperature, K
T_{feed}	feed temperature, K
v	superficial gas velocity, m/s
w	weight fraction
x	mole fraction
z	axial coordinate, m
Z_0	beginning of the insulation box, m
Z_L	end of the insulation box, m

Greek letters

α	heat transfer coefficient, $J/m^2/K/s$
ε	porosity
ζ	Conversion
η	particle effectiveness factor
η	viscosity, $kg/m/s$
λ	thermal conductivity, $J/m/K/s$
λ_{bed}	thermal conductivity of a quiescent packed bed, $J/m/K/s$
λ_{eff}	effective thermal conductivity, $J/m/K/s$
ρ	density, kg/m^3
ρ_{bulk}	bulk density of packed bed, kg/m^3
τ	residence time, s
τ	tortuosity
ϕ_v	flow rate, l/min (STP)
φ	thiele modulus

Subscripts

I	CH_4 combustion
II	steam reforming of CH_4
III	CO_2 reforming of CH_4
air	air
by-pass	by-pass
cat	catalyst
g	gas phase
h	hole
i	inner
in	inlet
o	outer
out	at the outlet
s	solid
total	total flow

Superscripts

$\ominus$	at standard pressure (10^5 Pa)
air	air
i	insulation layer
i–air	from the insulation layer to the air
s	shell
s–sw	from the shell to the shell wall
sw	shell wall
sw–i	from the shell wall to the insulation layer
sw–air	from the shell wall to the air
t	tube
tw	tube wall

Appendix A. Reaction kinetics of CH₄ combustion in air over a Pt/Al₂O₃ combustion catalyst

In a previous contribution, in which the conceptual feasibility of the RFCMR concept with porous membranes was investigated with a modelling study (Smit et al., 2005b), the reaction kinetics determined by van Sint Annaland (2000) were used to model the combustion of CH_4 in air. Although in this study very similar reaction rates were observed for fresh catalyst particles, a significant decrease in catalyst activity was observed during the experiments until a relatively steady state was reached. This decrease in activity was caused by the very high temperatures at which the RFCMR demonstration unit was operated, which resulted in Pt losses and sintering and hence deactivation of the catalyst. Therefore, to accurately describe the CH_4 combustion in the reactor model of the RFCMR demonstration unit, the reaction kinetics of the aged catalyst were determined experimentally. The experimental set-up, operating procedures and experimental results are shortly described in this appendix.

A.1. Experimental set-up and procedures

To determine the reaction kinetics of CH_4 combustion in excess air on a Pt/Al₂O₃ catalyst an experimental set-up was used, which was specifically designed to measure reaction kinetics. It consists of a quartz glass U-shaped tube, which is placed inside a heated fluidised bed to keep the catalyst bed at constant temperature (measured with a thermocouple). The gas feed flows to the U-shape tube were controlled with mass-flow controllers. The outlet composition was analysed with a Micro-GC (Varian, CP-4900), which has three separate columns. The first column was a Molsieve 5 Å column with He as carrier gas and was used to measure the O_2, N_2, CH_4 and CO mole fractions. The second column was also a Molsieve 5 Å column but with N_2 as carrier gas to measure the H_2 mole fraction. The third column was a PoraPlot Q column with He as carrier gas to measure the CO_2 and H_2O mole fractions. The Micro-GC has a very high sensitivity (to the ppm level) and the relative error in the measured concentration was typically 1–2%. A flow-sheet of the kinetics set-up is given in Fig. A1. The Pt/Al₂O₃ particles were crushed and sieved to obtain particles with a size of 212–500 μm. Prior to the experiments a sample of catalyst was weighed (about ±0.04 g) and placed inside the U-shape tube. Subsequently, the sample was heated up in the fluidised bed under inert conditions (N_2) and was kept at a temperature of about 1100 K for about 15 h before the measurements were started.

As was shown by van Sint Annaland (2000), the CH_4 reaction rate is linearly proportional to the CH_4 concentration for very low CH_4 fractions in excess air. Because O_2 is present in large excess, the O_2 concentration can be considered constant. Assuming ideal plug flow behaviour in the catalyst bed, the CH_4 mass balance can be written as

$$\phi_v \frac{\partial c_{CH_4}}{\partial z} = -\rho_{cat} k c_{O_2,in} c_{CH_4}. \tag{A.1}$$
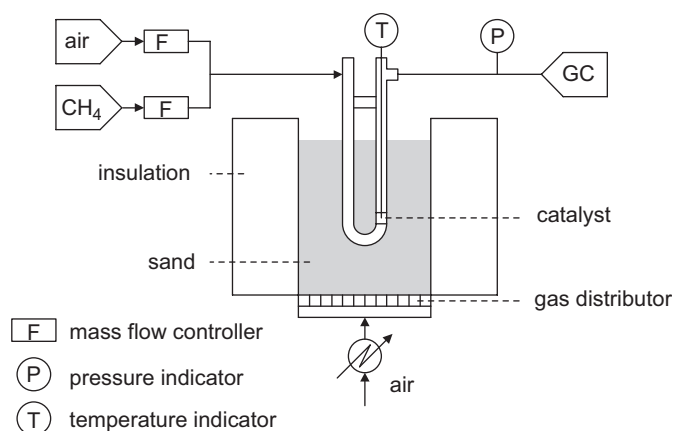

Fig. A.1. Flow-sheet of the kinetics set-up.

Integration over the catalyst bed yields

$$c_{CH_4,out} = c_{CH_4,in} \exp(-\rho_{cat} c_{O_2,in} \tau), \tag{A.2}$$

where

$$\tau = \frac{m_{cat}}{\phi_v \rho_{cat}}. \tag{A.3}$$

Rewriting Eq. (A.2) in terms of the CH_4 conversion then gives

$$k = \frac{-\ln(1 - \zeta_{CH_4})}{\tau \rho_{cat} c_{O_2,in}}. \tag{A.4}$$

From this equation the CH_4 reaction rate constant, k, can be determined by measuring the CH_4 conversion. For the temperature dependency of the reaction rate constant an Arrhenius-type expression was assumed

$$k = A \exp\left(-\frac{E_a}{R_g T}\right). \tag{A.5}$$

By plotting $\ln(k)$ versus $1/T$ the activation energy, E_a, and the pre-exponential factor, A, can be determined.

A.2. Experimental results

In Fig. A2 the reaction rate of the CH_4 combustion in air over the aged Pt/Al₂O₃ catalyst is given as function of the temperature for CH_4 inlet fractions of 0.005 and 0.01. The CH_4 conversion was less than 15% for all measurements so the influence of back-mixing and axial temperature profiles should be relatively small. From the slope and intercept of the trend line through the measured data points in Fig. A2 the activation energy and pre-exponential factor were calculated as 168 kJ/mol and 1.071×10^7 m⁶/kg/s/mol, respectively.

Also included in Fig. A2 is the reaction rate that was extrapolated from the reaction kinetics measured by van Sint Annaland (2000). The reaction rates measured in this study are about a factor 1.5–3 lower than those extrapolated from the kinetic parameters determined by van Sint Annaland (2000), while the activation energy was much higher, 168 versus 98.5 kJ/mol .
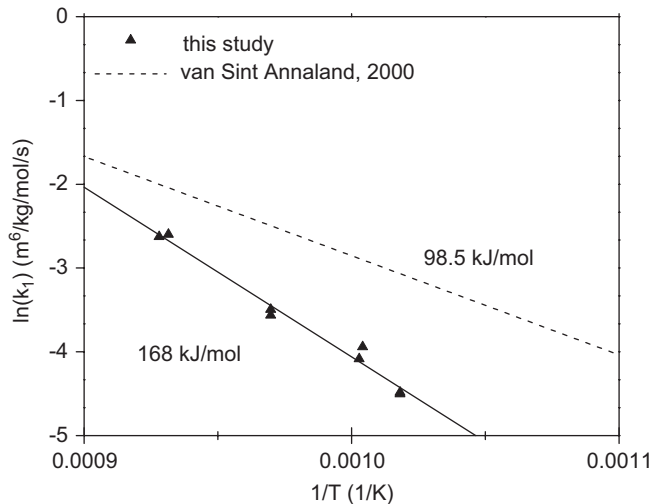
Fig. A.2. Reaction rate of CH_4 combustion in air over a Pt/Al_2O_3 combustion catalyst as a function of the temperature measured in this study (markers) and extrapolated from the kinetic expressions determined by van Sint Annaland (2000) (dashed line).
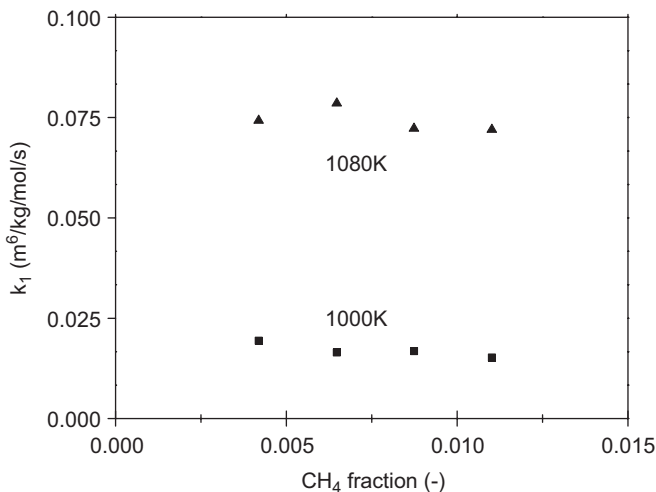

Fig. A.3. Reaction rate of CH_4 combustion in air over a Pt/Al_2O_3 combustion catalyst as a function of the CH_4 inlet fraction for different temperatures.

An explanation for the discrepancy in the activation energy could be that the reaction rates were measured in a different temperature range (1000–1100 K) in this study compared to the range (700–900 K) studied by van Sint Annaland (2000). (Trimm and Lam, 1980) also observed different activation energies for different temperature ranges at lower temperatures. Another explanation is that at higher temperatures also homogeneous gas phase reactions contributed to the observed reaction rate resulting in a higher apparent activation energy. Furthermore, also aging of the catalyst (sintering, changes in the pore system, loss of certain active sites, etc.) could have altered the apparent activation energy.

To verify the assumption that the CH_4 reaction rate is linearly proportional to the CH_4 concentration, the CH_4 conversion was measured as a function of the CH_4 inlet fraction for different temperatures. As is shown in Fig. A3, the reaction rate constant is indeed independent of the CH_4 concentration for low CH_4 inlet fractions. Finally, it should be noted that the contribution of homogeneous gas phase reactions is implicitly taken into account in the lumped reaction kinetics.

References

Aubé, F., Sapoundjiev, H., 2000. Mathematical model and numerical simulations of catalytic flow reversal reactors for industrial applications. Computers & Chemical Engineering 24 (12), 2623–2632.

Bird, R.B., Stewart, W.E., Lightfoot, E.N., 2002. Transport Phenomena. second ed. Wiley, New York.

Daubert, T.E., Danner, R.P., 1985. Data Compilation Tables of Properties of Pure Compounds. American Institute of Chemical Engineers, New York.

Dixon, A.G., Creswell, D.L., 1979. Theoretical prediction of effective heat-transfer parameters in packed-beds. A.I.Ch.E. Journal 25 (4), 663.

Edwards, M.F., Richardson, J.F., 1968. Gas dispersion in packed beds. Chemical Engineering Science 23 (2), 109–123.

Ergun, S., 1952. Fluid flow through packed columns. Chemical Engineering Progress 48 (2), 89–94.

Gunn, D.J., 1978. Transfer of heat or mass to particles in fixed and fluidized beds. International Journal of Heat and Mass Transfer 21 (4), 467–476.

Gunn, D.J., Misbah, M.M.A., 1993. Bayesian estimation of heat transport parameters in fixed beds. International Journal of Heat and Mass Transfer 36 (8), 2209–2221.

Karditsas, P.J., Baptiste, M.J., 2005. Thermal and structural properties of fusion related materials. URL ⟨http://www-ferp.ucsd.edu/PANOS/⟩.

Reid, R.C., Prausnitz, J.M., Poling, B.E., 1987. The Properties of Gases and Liquids. fourth ed. McGraw-Hill, Inc., New York.

Smit, J., 2006. Reverse flow catalytic membrane reactors for energy efficient syngas production. Ph.D. Thesis, University of Twente, Enschede, The Netherlands.

Smit, J., Bekink, G.J., van Sint Annaland, M., Kuipers, J.A.M., 2005a. A reverse flow catalytic membrane reactor for the production of syngas: an experimental study. International Journal of Chemical Reactor Engineering 3 (A12),

Smit, J., van Sint Annaland, M., Kuipers, J.A.M., 2005b. Feasibility study of a reverse flow catalytic membrane reactor with porous membranes for the production of syngas. Chemical Engineering Science 60 (24), 6971–6982.

Smit, J., van Sint Annaland, M., Kuipers, J.A.M., 2005c. Grid adaptation with weno schemes for non-uniform grids to solve convection dominated partial differential equations. Chemical Engineering Science 60 (10), 2609–2619.

Thoenes, D., Kramers, H., 1958. Mass transfer from spheres in various regular packings to a flowing fluid. Chemical Engineering Science 8 (3–4), 271–283.

Trimm, D.L., Lam, C.-W., 1980. The combustion of methane on platinum-alumina fibre catalysts—1: kinetics and mechanism. Chemical Engineering Science 35 (6), 1405–1413.

van de Beld, B., Westerterp, K.R., 1996. Air purification in a reverse-flow reactor: model simulations vs. experiments. A.I.Ch.E. Journal 42, 1139–1148.

van Sint Annaland, M., 2000. A novel reverse flow reactor coupling endothermic and exothermic reactions. Ph.D. Thesis, University of Twente, Enschede, The Netherlands.

Vortmeyer, D., 1989. Packed bed thermal dispersion models and consistent sets of coefficients. Chemical Engineering and Processing 26 (3), 263–268.

Westerterp, K.R., van Swaaij, W.P.M., Beenackers, A.A.C.M., 1984. Chemical Reactor Design and Operation. Wiley, New York.

Zehner, P., Schlünder, E.U., 1970. Wärmeleitfähigkeit von schüttingen bei mässigen temperaturen. Chemie Ingenieur Technik 42 (14), 933–941.